RESEARCH ARTICLE

J. Xie, Z. Ren, H. Zhou, J. Zhou,
W. Liu, C. Lee* 2401582

Artificial Intelligence-Enhanced "Photonic Nose" for Mid-Infrared Spectroscopic Analysis of Trace Volatile Organic Compound Mixtures

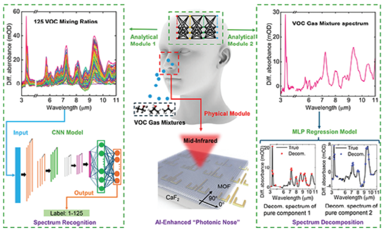

Molecular identification of volatile organic compounds (VOCs) plays an important role in various applications. Herein, an artificial intelligence-enhanced "photonic nose" is proposed for mid-infrared spectroscopic analysis of trace VOC gas mixtures. With low limits of detections, high-accuracymixture classification, and low-deviation component concentration predictions, this work paves the way for next-generation intelligent sensing platforms for environmental monitoring and smart framing.

ADVANCED OPTICAL MATERIALS
www.advopticalmat.de

Artificial Intelligence-Enhanced “Photonic Nose” for Mid-Infrared Spectroscopic Analysis of Trace Volatile Organic Compound Mixtures

*Junsheng Xie, Zhihao Ren, Hong Zhou, Jingkai Zhou, Weixin Liu, and Chengkuo Lee**

Molecular identification of volatile organic compounds (VOCs) plays an important role in various applications including environmental monitoring and smart farming. Mid-infrared (MIR) fingerprint absorption spectroscopy is a powerful tool to extract chemical-specific features for gas identification. However, the detection and recognition of trace VOC gas mixtures remain challenging due to their intrinsic weak light–matter interaction and highly overlapped absorption spectra. Here, an artificial intelligence-enhanced “photonic nose” for MIR spectroscopic analysis of trace VOC gas mixtures is proposed. To enhance the sensing performance by increasing bandwidth and sensitivity, the “photonic nose” is designed to employ coupled multi-resonant plasmonic nanoantennas to cover MIR molecular fingerprints, coated with metal–organic frameworks as the gas enrichment layer. Low limits of detection are achieved (IPA: 1.99 ppm, ethanol: 3.43 ppm, and acetone: 9.82 ppm). With machine learning, a high classification accuracy of 100% is realized for 125 mixing ratios (IPA, ethanol: both 5 concentrations, 0–130 ppm; acetone: 5 concentrations, 0–201 ppm), and low-deviation component concentration predictions of root-mean-squared error within 10 ppm are achieved for IPA and ethanol (both 0–130 ppm) under interference from 50 ppm acetone. The work paves the way for intelligent sensing platforms for environmental monitoring and smart framing.

1. Introduction

Volatile organic compounds (VOCs) are a group of organic compounds characterized by their propensity to transition into the gas phase from solid or liquid phases at room temperature, owing to the high vapor pressures.[1,2] Various VOCs can be found in daily activities, such as industrial emissions, automobile exhaust, and human exhalation.[3–6] The detection of VOCs holds significant importance in a wide range of fields, including environmental monitoring and smart farming.[7–10] Electrical and optical sensors are two common detection platforms for gas sensing. In the past few years, electrical sensors (“electronic nose”) have been widely reported for VOC sensing.[11–13] However, the performance of electrical sensors and refractive index (RI)-based optical sensors in identifying gas molecules is difficult for these sensors as the sensing signals (e.g., electrical properties or resonance wavelength) in these devices are not directly correlated with the chemical structures of VOC gas molecules.[14–16] Recently, surface-enhanced infrared absorption (SEIRA)-based VOC gas sensors have attracted great interest due to their label-free and nondestructive nature as well as their potential for molecular identification by leveraging molecular fingerprint absorption spectra.[17–20] However, the detection and recognition of trace VOC gas mixtures still remain challenging due to their intrinsic weak light–matter interaction and highly overlapped absorption spectra.

Nanoantennas, the artificial subwavelength periodic structures, offer immense design flexibility in engineering optical properties.[21–24] The metal plasmons can achieve extreme light confinement, strongly enhance the near-field intensity by several orders, and hence increase the light–matter interactions.[25,26] To address the challenge of high-accuracy classification and component concentration prediction of trace VOC gas mixtures, acquiring more molecular characteristic information and realizing low LoD are required. Multiresonant nanoantennas have been reported to simultaneously enhance the different vibrational fingerprints for distinguishing multiple molecules.[27–30] Recently, biosensing based on multiresonant nanoantenna has been demonstrated for various applications, such as COVID-19 virus identification, chiral molecule structure identification, brain tissue detection, etc.[31–34] However, there is a technological challenge to extend solid/liquid-sample sensing to discrete gas

J. Xie, Z. Ren, H. Zhou, J. Zhou, W. Liu, C. Lee
Department of Electrical & Computer Engineering
National University of Singapore
4 Engineering Drive 3, Singapore 117583, Singapore
E-mail: elelc@nus.edu.sg

J. Xie, Z. Ren, H. Zhou, J. Zhou, W. Liu, C. Lee
Center for Intelligent Sensors and MEMS
National University of Singapore
4 Engineering Drive 3, Singapore 117583, Singapore

C. Lee
NUS Graduate School- Integrative Sciences and Engineering Programme (ISEP)
National University of Singapore
Singapore 117583, Singapore

The ORCID identification number(s) for the author(s) of this article can be found under https://doi.org/10.1002/adom.202401582

DOI: 10.1002/adom.202401582

molecules as smaller intermolecular forces of gas molecules result in their random distribution in free space and the evanescent field of nanoscale antennas restrict their ability to sense more gas molecules (the near-field enhancement of plasmonic nanoantennas is dominant within 100 nm).[35] Currently, a common method used to enhance the sensitivity of nanoantenna-based sensors is by reducing the gap between adjacent nanoscale antennas to increase the near-field intensity thus enhancing the light–matter interactions.[36,37] However, the huge cost and high fabrication requirement impede this method for further development. An alternative method is to employ molecule enrichment layers to amplify the surface gas concentration.[38,39] Various materials have been reported for physical or chemical adsorption of VOCs including activated carbon,[40] graphene oxide,[41] carbon nanotube,[42] metal–organic frameworks (MOFs),[43] silica gel,[44] organic polymer.[45] Among them, MOFs have emerged as compelling candidates for gas enrichment layers of plasmonic sensors for their exceptional surface area, ultrahigh porosity, and tunable structures.[46–48] By leveraging the attractive properties of MOFs, it becomes possible to concentrate trace gases within the sensing region, thereby amplifying the signal and facilitating more robust identification. However, the task of classification and component concentration prediction of mixtures remains arduous due to the overlapping vibrational modes.

Artificial intelligence (AI) has emerged as a potent tool for extracting intricate features from complex spectroscopic data, enabling the discernment of subtle molecular nuances that elude conventional analysis methods.[49–55] Through feasible big data processing utilizing machine learning techniques, such as principal component analysis (PCA), support vector machines (SVM), convolutional neural networks (CNN), and multilayer perceptron (MLP) regression, AI can reinforce the characteristic gas sensing dataset.[56–61] Thus, the AI-enhanced methodology would be a promising solution for trace VOC gas mixture analysis in environmental monitoring, where identifying trace-amount molecules requires rapid response, high accuracy, anti-interference, and high sensitivity.[62–65]

Here, we propose an AI-enhanced "photonic nose" for the mid-infrared (MIR) spectroscopic analysis of trace VOC gas mixtures. A coupled multiresonant plasmonic nanoantenna (CMRPN) is designed to cover the VOC molecular fingerprints in the MIR range, coated with a layer of MOF is employed as the gas enrichment layer to form the MOF-hybrid CMRPN (MCMRPN). Three widely used VOC molecules (IPA, ethanol, acetone) are selected to demonstrate the sensing performance of our MCMRPN platform, and low LoDs down to single-digit ppm are achieved. Deep machine learning models are utilized to analyze the multidimensional data from the MCMRPN platform due to the considerable overlap of absorbance peaks among VOC gas molecules. A CNN model is employed to conduct the classification of mixtures, and a high accuracy of 100% is realized for 125 mixing ratios of three VOCs (IPA: 5 concentrations from 0 to 130 ppm; ethanol: 5 concentrations from 0 to 130 ppm, and acetone: 5 concentrations from 0 to 201 ppm). Additionally, an MLP model is utilized for decomposing the spectra of mixtures into spectra of pure components. We successfully decompose the spectra of pure forms components from the remaining 20% unknown mixing combinations by training on the spectral information of only 80% of the concentration combinations. Following spectrum decomposition, a linear regression model is applied to predict the component concentrations. Remarkably, our methodology demonstrates a low-deviation prediction result within 10 ppm of root-mean-square-error (RMSE) is realized for IPA and ethanol both in the range of 0–130 ppm even under interference from 50 ppm acetone. Our work holds great potential to pave the way for diverse analytical scenarios including environmental monitoring and smart farming applications.

2. Results and Discussions

2.1. Working Mechanisms of Molecular Identification of VOCs Using AI-Enhanced "Photonic Nose"

Figure 1a demonstrates the concept of the proposed AI-enhanced "photonic nose", which consists of two modules: a physical module and an analytical module. Figure 1b shows the physical module of the proposed "photonic nose". As demonstrated in Figure 1b(i), the "photonic nose" comprises a CMRPN array deposited on the IR glass substrate CaF_2. After that, a layer of MOFs, which served as gas molecule trapping material, was spin-coated on top of the gold nanoantenna. The MOF used here is ZIF-67, which is physically and chemically stable and mainly captures gas molecules through physical adsorption. The proposed CMRPN consists of a pair of split-ring resonators (SRRs) symmetrically positioned on the left and right sides of the nanorod (NR) antenna. Figure 1b(ii) illustrates the schematic representation of resonance modes of the proposed CMRPN, double-u, and nanorod metaunit coupled to incident MIR light under vertical (90°) and horizontal (0°) polarization. Resonance mode λ_1 arises from the secondary resonance at a short wavelength (λ_7) of SPRs under 90° polarization. Modes λ_2 and λ_3 are excited by the plasmonic bright-dark coupling between the NR and SPRs, explicable through temporal coupled-mode theory (TCMT). When excited with 90° polarization, the elementary radiative electric dipolar resonance of the center NR acts as the bright mode (λ_6), while the nonradiative fundamental magnetic modes of the side SRRs function as the dark mode (the resonant wavelength position can be disclosed by using a 0° polarization, closely aligning with λ_5). Plasmonic mode coupling occurs when λ_6 and λ_5 are proximate, resulting in spatially overlapping yet spectrally split plasmonic resonances of λ_2 and λ_3 (Figure 1b(iii). See theoretical analysis in Note S1, Supporting Information). An additional resonance mode λ_4 is excited by simply adjusting the incident polarization angle to 0°, effectively filling the spectral gap between λ_2 and λ_3. Consequently, four resonant peaks are achieved, densely covering our target fingerprint range. Under illumination, light is localized in a small volume, forming hot spots due to metal plasma localization, and the near-field intensity is significantly enhanced by several orders (Many VOCs serve as biomarkers for environmental monitoring, and accurate detection of VOC mixtures and their components are needed to facilitate next-generation sensors for environmental monitoring. However, achieving classification and component concentration prediction of VOC gas mixtures (especially at low concentrations) is challenging due to the overlap of molecular vibration modes. The analytical module of our "photonic nose" is demonstrated in Figure 1c. A powerful deep machine learning model CNN was employed for the classification of trace VOC gas mixtures with 125 (5 × 5 × 5) mixing

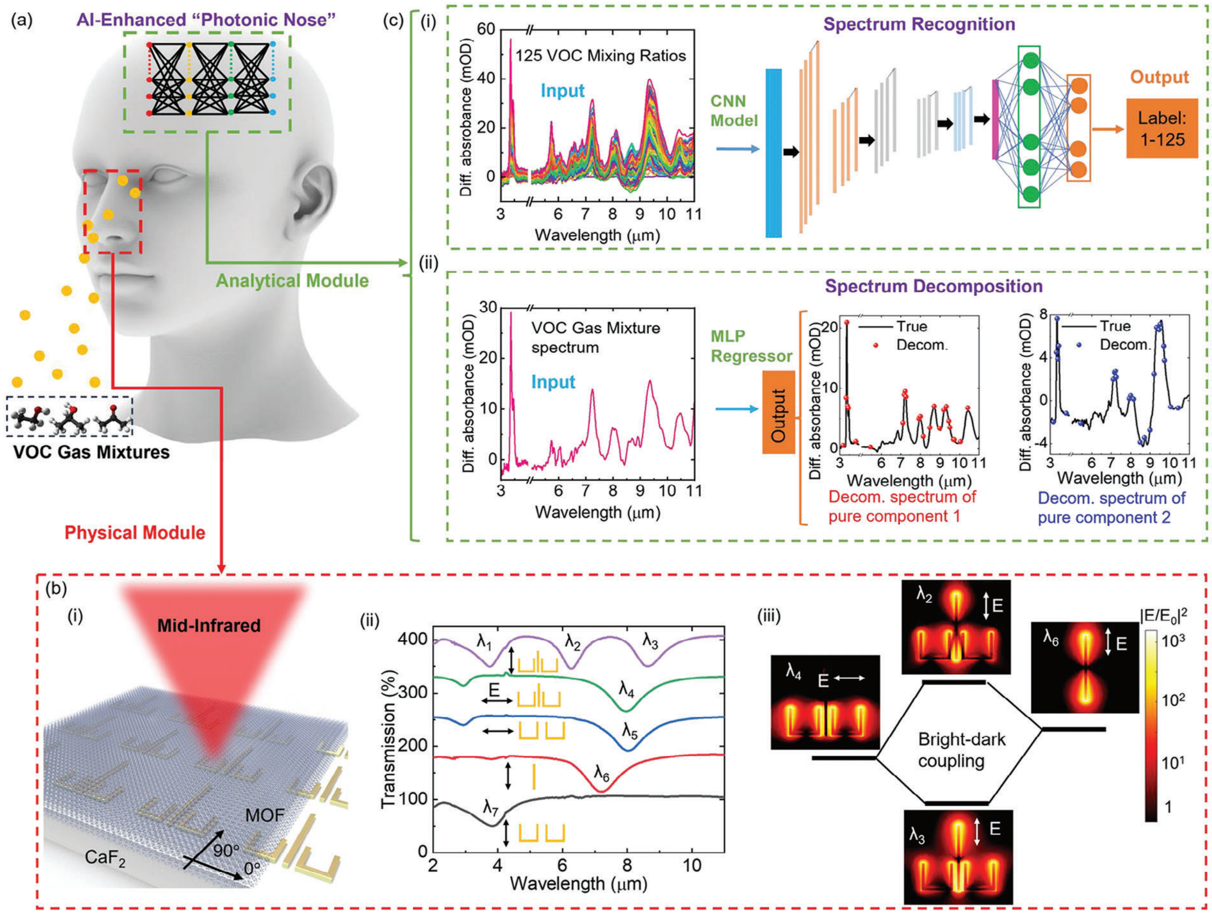

Figure 1. The schematic diagram of AI-enhanced "photonic nose" for trace VOC gas mixture analysis. a) Schematic diagram of the concept of AI-enhanced "photonic nose", which consists of two modules: physical module and analytical module. b) Physical module of the proposed "photonic nose": MCMRPN. b(i) Schematic depiction of MCMRPN, consisting of gold nanoantenna on CaF_2 substrate and a spin-coated layer of MOF. b(ii) Schematic representation of resonance modes of the CMRPN, double-u, and nanorod metaunit coupled to the incident MIR light. b(iii) Schematic diagram of bright-dark coupling of CMRPNs and respective near-field intensity under vertical polarization. c) Analytical module of the proposed "photonic nose": machine learning. c(i) Classification of trace VOC gas mixtures with 125 mixing ratios (IPA, ethanol, acetone, and their combinations) employing the CNN model. c(ii) Schematic representation of the process of spectrum decomposition using the MLP regression model.

ratios of three VOC gas (IPA: 5 concentrations, ranging from 0 to 130 ppm; ethanol: 5 concentrations, ranging from 0 to 130 ppm; acetone: 5 concentrations, ranging from 0 to 201 ppm). The spectra of 125-class mixtures were used as input for the CNN model, and the output results were the respective predicted labels. Additionally, an MLP regression model was applied to decompose the mixture spectrum into pure forms of components. Figure 1c(ii) illustrates the schematic representation of the process of spectrum decomposition using the MLP regression model. The input of the MLP regression model was the multidimensional spectrum data of the VOC mixture spectrum and the outputs were the decomposed spectra of selected components with interest. Here, the example of input is the spectrum of the mixture of three VOC molecules (IPA: 100 ppm; ethanol: 40 ppm; and acetone: 50 ppm), and the outputs are decomposed spectrum of 100 ppm IPA (pure component 1) and 40 ppm ethanol (pure component 2), respectively, and 50 ppm acetone here is the interference. Based on the MLP-decomposed spectrum of pure forms, component concentration prediction can be further achieved by utilizing a linear regression model.

2.2. Analysis of CMRPN

As demonstrated in **Figure 2**, the spectral position of each resonance peak is tunable by adjusting the geometric parameters of the CMRPN. We fabricated a series of CMRPN arrays with varying structural parameters (Optical images and SEM images in Figure S2, Supporting Information). As illustrated in Figure 2a, excited by vertical (90°) polarization, the resonance peaks λ_2 and λ_3 exhibit redshifts as the length of the center NR increases, attributable to the increase in the fundamental dipole resonant wavelength, while λ_1 remains nearly unchanged, as it is solely related to L_1. Similarly, redshifts of λ_2 and λ_3 can be achieved by increasing the length of L_1, as depicted in Figure 2b. On the contrary, λ_1 also undergoes a redshift when L_1 is increased, corresponding to the redshift of the secondary resonance peak

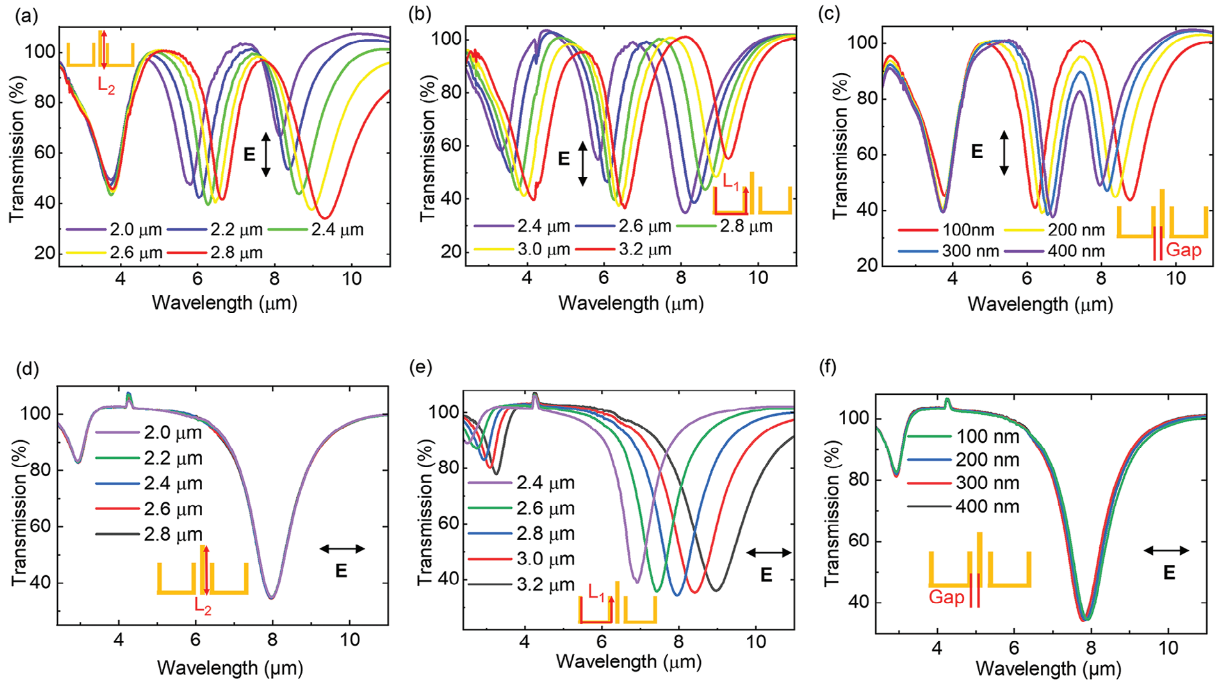

Figure 2. Analysis of CMRPN. a–c) Experimental spectra of CMRPNs under incident light with 90° polarization with varying L_2, L_1, and gap, respectively. The inset image illustrates the structural parameters. d–f) Experimental spectra of CMRPNs under incident light with 0° polarization with varying L_2, L_1, and gap, respectively.

of SRR. Furthermore, adjusting the gap between the SRRs and NR enables control over the bright-dark coupling strength (μ), resulting in different wavelength spacings of the two resonance wavelengths λ_2 and λ_3, as demonstrated in Figure 2c. When the gap is small, the coupling strength increases significantly due to the near-field coupling caused by the proximity between the SRR and NR. While only the fundamental resonance mode λ_4 of the SRRs is excited under the illumination of horizontal polarization (0°). As demonstrated in Figure 2d–f, λ_4 almost maintains the same position with changes in L_2 and the gap, while redshifts with increasing L_1, as the resonance mode λ_4 is from the radiative electric dipolar resonance λ_5 of the SRRs, which is only related to L_1.

2.3. Demonstration of Trace VOC Gas Sensing with MCMRPN Platform

Figure 3 illustrates the sensing performance of our MCMRPN platform for VOC gas detection. We fabricated an ulu nanoantenna array with dimensions L_1 = 2.5 μm, L_2 = 2.4 μm, gap = 100 nm, and the period in x and y direction $P_x = P_y$ = 3.5 μm. A layer of MOF (ZIF-67) was spin-coated atop the metal nanoantenna (Figure 3a). The ZIF-67 is zeolitic imidazolate framework, which have exceptional chemical and thermal stability. The adsorption of VOCs of MOFs in the experiments is physical. The thickness of the MOF layer is a crucial factor for gas enrichment. The near-field intensity of the nanoantenna is predominantly enhanced within ≈100 nm. The AFM image of the cross-sectional thin film reveals that the thickness of the MOF layer is ≈550 nm, sufficient for molecule trapping (Figure S6, Supporting Information). As shown in Figure 3b, the MOF exhibits six representative IR peaks in the MIR range. After loading MOF, the corresponding sharp peaks are observed in the measured spectra of the MCMRPN platform under vertical and horizontal polarizations (Figure 3c). Three VOCs (IPA, ethanol, and acetone) were selected to evaluate the sensing performance of our MCMRPN platform. The schematic diagram of our optical measurement setup is illustrated in Figure S9 (Supporting Information). Nitrogen (N_2) served as the buffered gas, divided into four flows and finely controlled by mass flow controllers (MFCs). One flow comprises pure N_2, while the remaining three flows pass through 99.5% VOC solutions to generate respective VOC vapors. The N_2 gas flow and target VOC gas flows were controlled to enter the mixing chamber by respective MFCs and valves to generate VOC gas mixtures with different mixing ratios. The gases were uniformly mixed by a fan in the mixing chamber and then flowed out through the outlet and entered the gas cell, where our MCMRPN platform was located. The sampling state contains a gas cell and an FTIR to collect the spectra. As a proof-of-concept, we use the FTIR to measure the spectra. However, the optical components can be further miniaturized, and the on-chip integration can be realized for practical applications. Figure 3d depicts the spectral response (90° polarization) of our MCMRPN platform with varying IPA concentrations. Figure 3d(i) presents the measured transmission spectra of IPA over a wide concentration range (0–337 ppm). To consider all gas-induced spectral changes, the differential absorbance spectra in the MIR band are calculated as $-\log_{10}(T/T_0)$, where T and T_0 are the measured and baseline transmission, respectively. Figure 3d(ii) illustrates the respective differential absorbance spectra extracted from Figure 3d(i). The intensity of differential absorbance increases with the

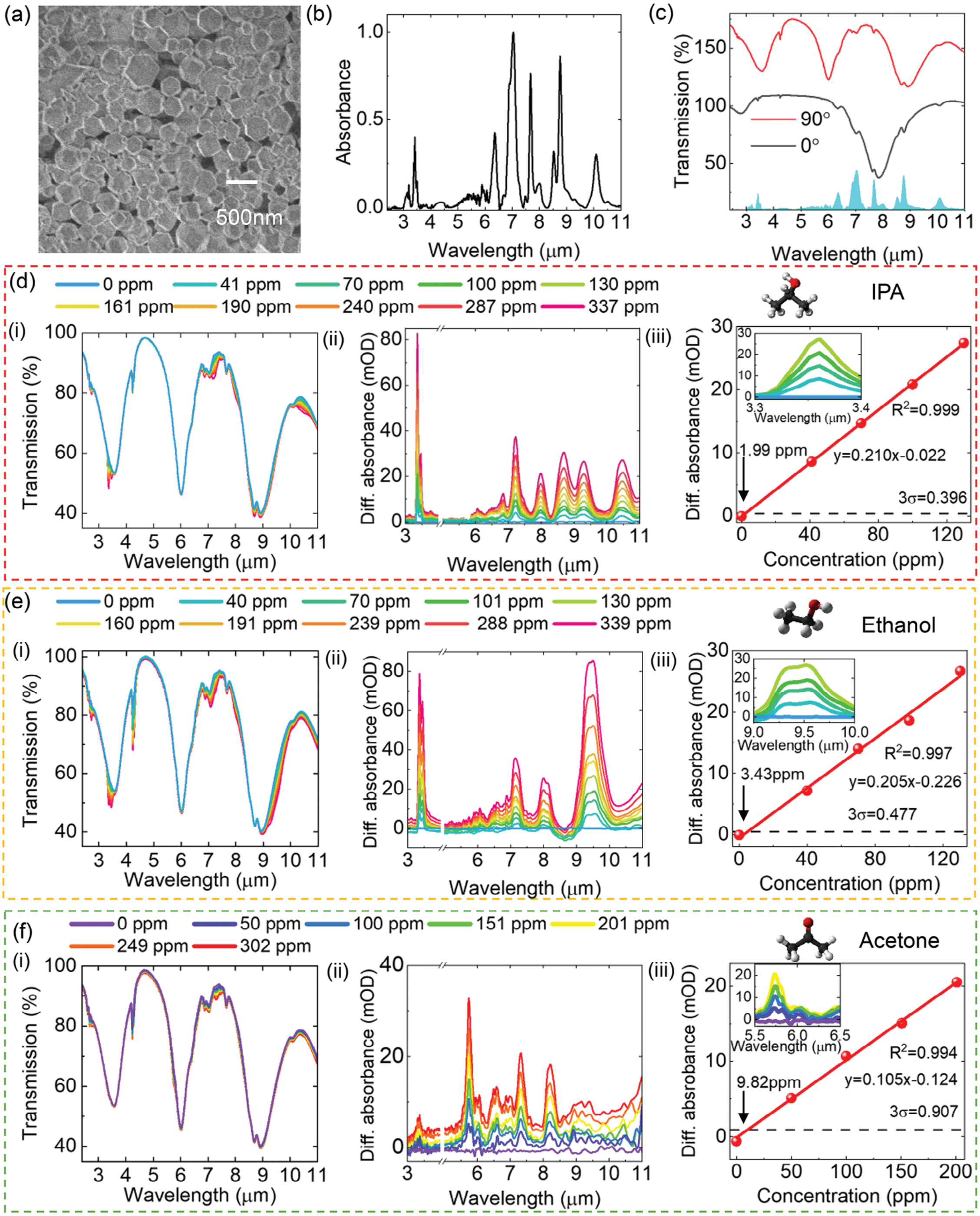

Figure 3. Demonstration of trace VOC gas sensing with MCMRPN platform. a) SEM image of MOF (ZIF-67). b) Measured IR absorbance of used MOF (ZIF-67). c) Measured spectra of CMRPN array with MOF under the illumination of 0° and 90° polarized light. The bottom inset is the absorbance peaks of MOF from 3b. d) Sensing results of IPA. d(i) Measured spectral response of IPA with varying concentrations (0–337 ppm) using the MCMRPN platform (90°). d(ii) Corresponding differential absorbance of IPA of different concentrations, which is calculated as $-\log_{10}(T/T_0)$, where T and T_0 are the measured and baseline transmission. d(iii) Peak differential absorbance at 3.36 μm versus IPA concentration profile in a small IPA concentration range (0–130 ppm). The LoD is defined by the intersection of 3σ noise level and the linear fitting curve. Inset is the peak differential absorbance around 3.36 μm. e) Sensing results of ethanol. e(i) Measured spectral response of ethanol with varying concentrations (0–339 ppm) using the MCMRPN platform (90°). e(ii) Corresponding differential absorbance of ethanol of different concentrations. e(iii) Peak differential absorbance at 9.49 μm versus ethanol concentration profile in a small ethanol concentration range (0–130 ppm). Inset is the peak differential absorbance around 9.49 μm. f) Sensing results of acetone. f(i) Measured spectral response of acetone with varying wide-range concentrations (0–302 ppm) using the MCMRPN platform (90°). f(ii) Corresponding differential absorbance of acetone of different concentrations. f(iii) Peak differential absorbance at 5.74 μm versus acetone concentration profile in a small acetone concentration range (0–201 ppm). Inset is the peak differential absorbance around 5.74 μm.

rise in IPA concentration. Figure 3d(iii) demonstrates the peak absorbance at 3.36 μm wavelength in a smaller concentration range (0–130 ppm) of IPA. The left-top inset shows the zoom-in 3.3–3.4 μm absorbance spectrum of IPA from Figure 3d(ii). The peak absorbance values at 3.36 μm are extracted, showing a linear relationship with concentration in the range of 0–130 ppm. The sensitivity of the sensor, defined as the slope of the fitting curve, reaches 0.210 mOD ppm^{-1}. The LoD is crucial for evaluating the sensing behavior and is closely related to noise. The total noise is obtained by collecting the spectra of the MCMRPN platform 30 times using pure nitrogen and then extracting the signal fluctuations of these spectra. The noise of our MCMRPN platform is shown in Figure S10 (Supporting Information). The high noise level around 5.5–6.5 μm is due to the messy absorption of water vapor. Specifically, the noise level in the range of 3–4 μm wavelength is considered in IPA case. The LoD calculation is based on the 3σ principle, where σ is the highest noise level extracted in the range of 3–4 μm wavelength. The intersection points of the 3σ horizontal line and linear fitting curve show the LoD to be 1.99 ppm. Another point we need to highlight is that the enrichment effect of the MOFs can remain the same after repeated tests. We have repeated the measurement of 100 ppm ethanol using our MCMRPN devices for 50 times. The 50 absorption spectra are demonstrated in Figure S8 (Supporting Information). We need to clarify that many factors contribute to the fluctuations of the repeated tests, such as the stability of gas concentrations and gas flow, and the background noise. The variations of the MOF enrichment effect are smaller than the measured fluctuations. Figure 3e(i) illustrates the measured transmission spectral response of ethanol over the range of 0–339 ppm. Spectral changes mainly occur around the absorbance peaks of ethanol (3.3, 7.2, 8.0, and 9.5 μm). The respective differential absorbance of ethanol is depicted in Figure 3e(ii). The peak signals at 9.49 μm versus smaller ethanol concentrations range (0–130 ppm) are illustrated in Figure 3e(iii). The left-top inset shows the zoom-in 9–10 μm absorbance spectrum of ethanol from Figure 3e(ii). The peak absorbance linearly rises with increasing ethanol concentration. The linear fitting results show the sensitivity of ethanol to be 0.205 mOD ppm^{-1}. Specifically, the noise level in the range of 9–10 μm wavelength is considered in the ethanol case, and the calculated LoD is down to 3.43 ppm. Similar experiments were conducted to investigate the sensing performance of acetone using our MCMRPN platform as illustrated in Figure 3f(i–iii). Clear peaks are observed around the molecular fingerprints of acetone (5.7, 7.3, and 8.3 μm). The results show that the sensitivity of acetone is 0.105 mOD ppm^{-1}. Noise level in the range of 5.5–6.5 μm wavelength is considered for the acetone case. The respective LoD of acetone is 9.82 ppm. The lower sensitivity of acetone compared to IPA and ethanol is due to the weak vibrational mode intensity and poor absorbance intensity of acetone in MOF as the acetone molecule size is bigger.

2.4. Classification of Trace VOC Gas Mixtures with Deep Machine Learning

We conducted a series of experiments to characterize the recognition capability for VOC gas mixtures of our MCMRPN platform. **Figure 4a** illustrates the measured absorbance signals of IPA, ethanol, acetone, and their combinations (The total concentration of all 7 classes of mixtures is fixed at 130 ppm). The absorbance peaks are highly overlapping due to the presence of the same methyl bond functional groups in these three VOC molecules as well as hydroxyl bonds in IPA and ethanol. These overlaps pose challenges for conventional data processing methods in clear distinction. Hence, we propose an AI-enhanced method to extract the unique characteristics of each class from the complex multidimensional data obtained from our MCMRPN platform. Figure 4b visualizes the three main principal components (PC) using PCA, which reduced the dimension number to three while retaining the main information. Seven classes of mixtures are clearly distinguished after PCA processing, of which each class was measured 50 times to ensure sufficient training data. Subsequently, a supervised machine learning model SVM performed the classification based on the three main PCs. SVM is originally a classification algorithm for two-group classification problems, and we transform our classification into a set of binary classification problems to distinguish seven different gas mixtures. Fifty groups of 3D PCA data for each class were divided into 40 groups for the training set and 10 groups for the testing set. Ultimately, the classification accuracy is 100% for all seven classes of mixtures (Figure 4c). The difficulty in distinguishing spectra intensifies when components with varying concentrations. Figure 4d depicts 125 classes of VOC gas mixtures with different mixing ratios, correlating each mixing ratio with labels 1−125 (Figure S12, Supporting Information). Figure 4e presents the measured absorbance spectra with overlapping absorbance peaks for 125 classes. Fifty spectra were measured for each class, and 6250 spectra in total. To address these complex mixture cases, a 1D CNN (1D-CNN) model was employed for classification. A 1D-CNN is a type of neural network specifically designed to process sequential data. Unlike the 2D-CNNs used for image processing, 1D-CNNs are applied to sequences, such as time series data, audio signals, text, or spectral data. 1D-CNN is computationally efficient for sequential data as it reduces the number of parameters compared to fully connected networks. 1D-CNN automatically learns and extracts relevant features from raw input data, eliminating the need for manual feature engineering. Figure 4f illustrates the detailed structure of the proposed 1D-CNN model. The training and testing sets were divided in a ratio of 1:4. The loss versus epoch number is plotted in Figure 4g, with the loss decreasing to 2.0×10^{-5} after 50 epochs. As shown in Figure 4h, a high accuracy of 100% is achieved in recognizing 125 classes of gas mixtures. These high-accuracy results validate the powerful ability of CNN, as well as the reliable and stable sensing performance of our MCMRPN platform.

2.5. Spectrum Decomposition and Component Concentration Prediction of Trace VOC Gas Mixtures with Deep Machine Learning

In addition to classification, it is crucial to extract individual spectrum information and component concentrations from VOC gas mixtures. However, decomposing the spectrum of mixtures presents challenges due to the overlapping absorbance spectra of components and the nonlinear superposition of spectra. This problem is exacerbated when trying to resolve the spectrum of

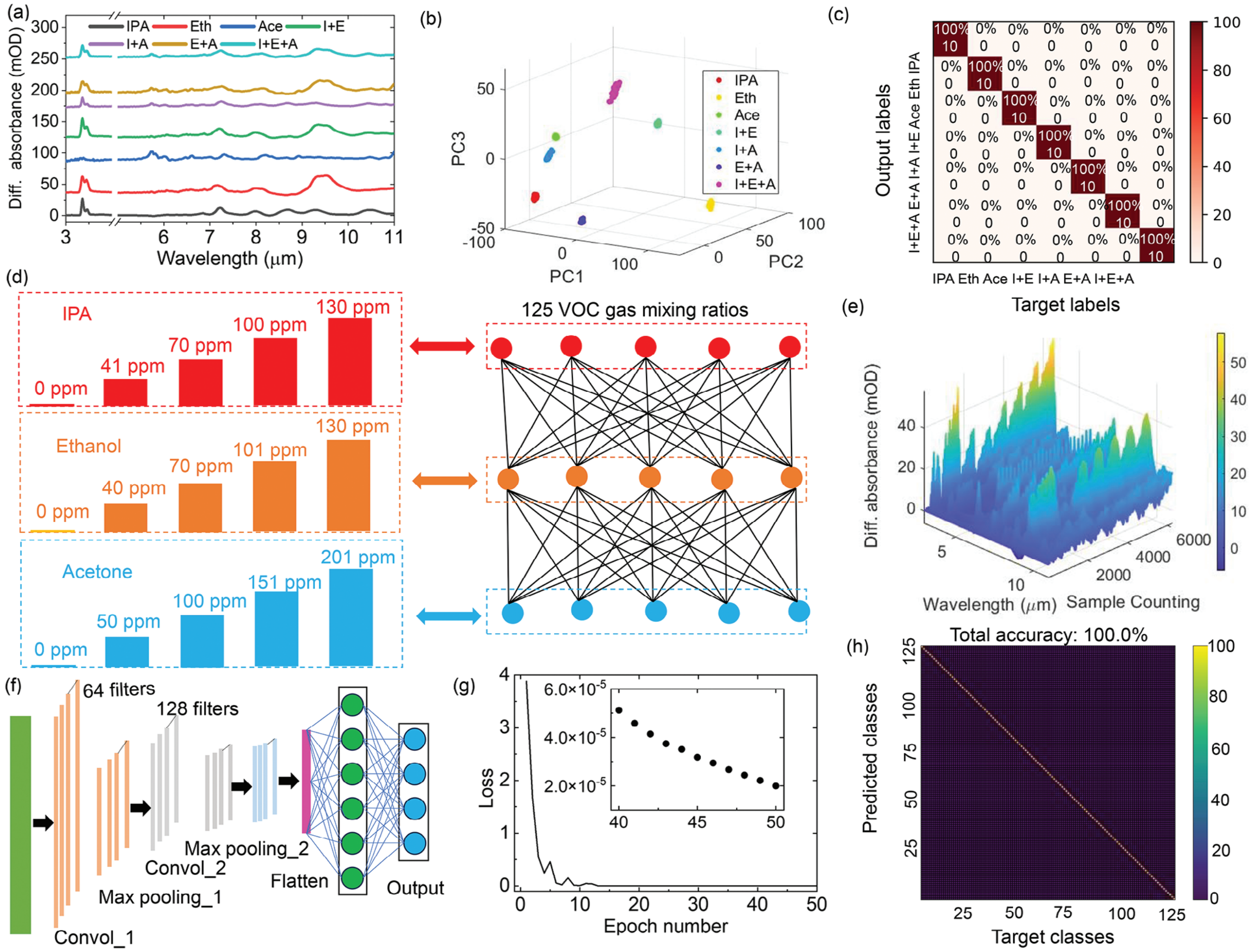

Figure 4. Demonstration of classification of trace VOC gas mixtures with deep machine learning. a) Measured absorbance spectra of different VOC analytes (IPA, ethanol, acetone, and their combinations) under incident light with 90° polarization. The total concentration of all 7 classes of mixtures is fixed at 130 ppm. b, c) Corresponding feature extraction and classification accuracy of different analytes by PCA and SVM. d) 125-class VOC gas mixtures with different mixing ratios. e) Absorbance spectra of 125 classes mixtures. Each class contains 50 spectra, and 6250 spectra in total. f) The detailed structure of the CNN training model. g) The training loss versus epoch number of the CNN model. The inset shows the loss values for epoch numbers from 40 to 50. h) Testing accuracy in identifying 125-class mixtures. The total accuracy is 100.0%.

selected components under interference from other gases. To address this challenge, we adopted an alternative model, MLP regression, to decompose mixture spectra and extract hidden spectrum information of components. MLP regressor is a type of feedforward artificial neural network used for regression tasks. Furthermore, the MLP regression model requires only a spectrum of each class to operate. Key Components of an MLP Regressor include the Input Layer, Hidden Layers, and Output Layer. The Mechanisms of an MLP Regressor include Forward Propagation, Backpropagation, and Training. During the training process, the loss function, gradient descent, and weight updates are utilized to enhance the model's predictions. In our scenario, IPA and ethanol were selected components of interest, while acetone served as an interference item. We prepared five concentrations of IPA and ethanol gases from 0 to 130 ppm. These gases are mixed in pairs to create 25 different mixture combinations (5 × 5). Each of these 25 combinations was then mixed with 0 and 50 ppm of acetone gas, respectively, resulting in a total of 50 (5 × 5 × 2) IPA-ethanol-acetone mixture combinations with acetone as the interference. **Figure** 5a illustrates the workflow of our MLP model. Figure 5b depicts the spectral decomposition of an example mixture of 70 ppm IPA, 70 ppm ethanol, and 50 ppm acetone using the MLP regression model. The input layer of MLP regression was the mixture spectrum of 934 wavelength points (934 × 1, Figure 5b(i)). In the training process, 40 of 50 spectra were randomly selected as the training dataset, and the ground truths (expected output) were set as the cascading of measured pure IPA and ethanol spectra at 25 selected wavelength points. As illustrated in Figure 5b(ii), two hidden layers with sizes of 256 and 128 were used to proceed with the input data. The size of the output layer was 50 × 1, of which the first 25 points were the absorbance spectrum values of 25 selected wavelength points and formed the decomposed spectrum of 70 ppm IPA (Figure 5b(iii)), while the last 25 points were the spectrum

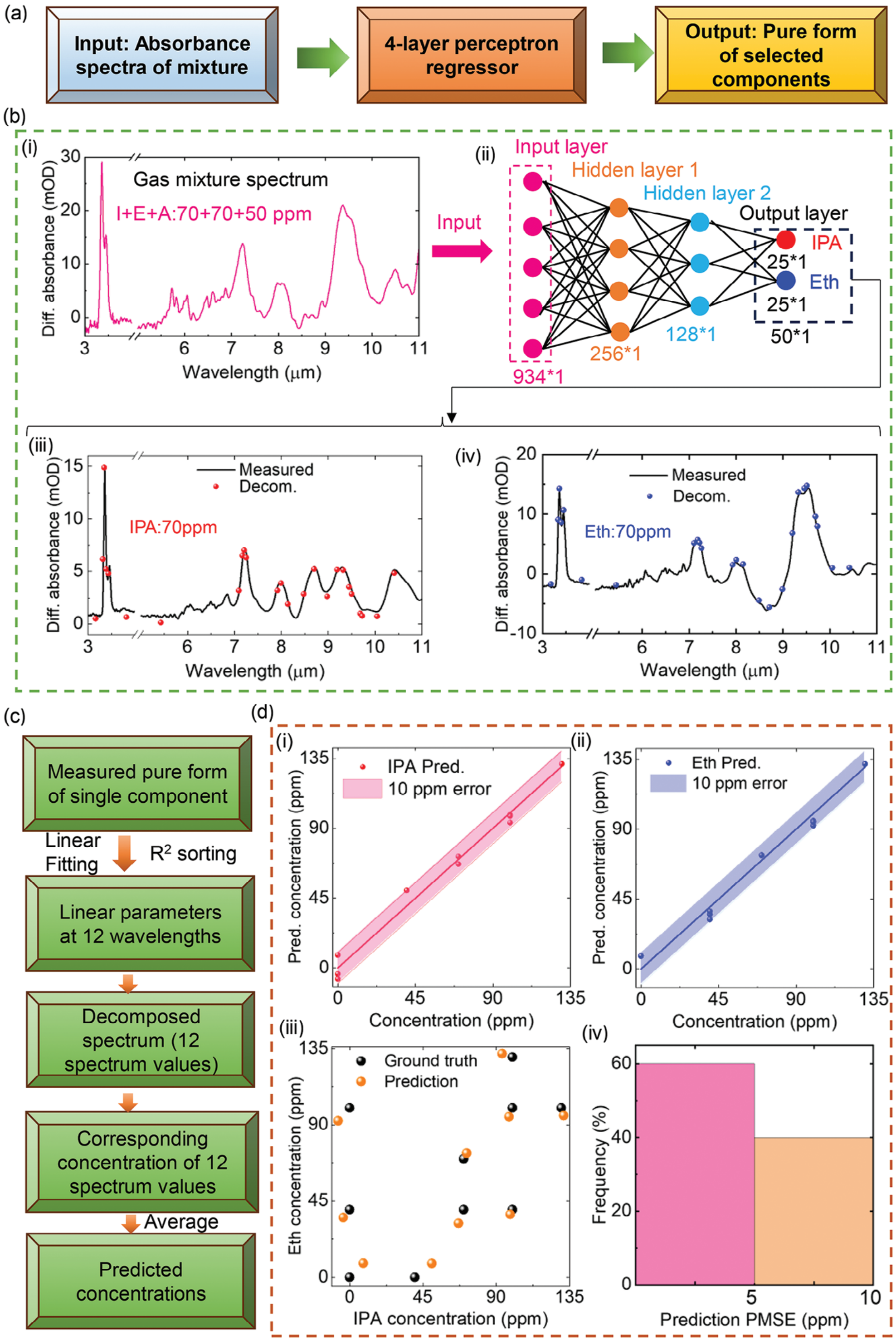

Figure 5. Demonstration of spectrum decomposition and component concentration prediction of trace VOC gas mixtures with deep machine learning. a) The workflow of the MLP regression model. b) Spectral decomposition of an example mixture of 70 ppm IPA, 70 ppm ethanol, and 50 ppm acetone using the MLP regression model. b(i) Spectrum of the mixture of 70 ppm IPA, 70 ppm ethanol, and 50 ppm acetone. b(ii) Detailed structure of the MLP regressor. Each layer is fully connected with the other. b(iii, iv) Respective decomposed pure form of 70 ppm IPA (red spheres, 25 × 1), 70 ppm ethanol (blue spheres, 25 × 1), from the output of the MLP regressor with their corresponding measured values (black curves, 934 × 1) for reference. The results shown here are from the testing process. c) Flowchart of predicting component concentration from the decomposed pure form (predicted spectrum). d) Concentration prediction results. d(i, ii) Prediction concentrations of IPA and ethanol, respectively. d(iii) Predicted concentration combinations (orange spheres) from the testing set with their corresponding correct concentration combinations (black spheres, ground truth) plotted on the 2D space. d(iv) Histogram of prediction RMSE for 10 mixing ratios in the test data set.

values of 25 identical wavelength points to form the decomposed spectrum of 70 ppm ethanol (Figure 5b(iv)). A mean square error (MSE) function was used in the MLP regression model as the loss function to measure the difference between the decomposed spectrum vectors (50×1) and the true vectors extracted from the measured spectrum values of respective pure VOC gas. As illustrated in Figure S13 (Supporting Information), by using an Adam Optimizer in Pytorch, the MSE loss gradually decreased with the increase of epoch number and finally down to 3.2×10^{-3}. Unlike the CNN having to experience all classes of data in the training process, the 40 mixture spectra in the training process of the MLP regressor only exhibit a subset of all concentration combinations, which means the concentration combinations carried by the 10 mixture spectra in the test data set are completely unknown to the MLP regressor. After spectrum decomposition, the concentration of components can be predicted by leveraging the MLP-decomposed spectrum (predicted spectrum). Figure 5c shows the process of concentration prediction. A linear regression model was applied to the spectra of a single pure component over 5 concentration ranges (0–130 ppm) at the identical 25 wavelength points as the decomposed spectra. Linear parameters (including slope and intercept) and R-squared values were obtained by a least-squares fitting method. Subsequently, among the 25 wavelength points, 12 points with higher R-squared values in the case of ethanol and IPA were selected. These parameters extracted from the measured spectrum were then employed in the decomposed spectrum to reverse-calculate the corresponding concentrations at these 12 wavelength points. Finally, the predicted concentration was derived by averaging these 12 concentrations. Figure 5d demonstrates the predicted concentrations of IPA and ethanol in the IPA-ethanol-acetone mixture for the test cases. All the predicted concentrations are in the range of ground truth± 10 ppm for IPA and ethanol (Figure 5d(i,ii), respectively). Figure 5d(iii) visually compares the ground truth (black spheres) with the predicted concentration combination (orange spheres) in the test dataset. The RMSE is often used to quantitatively describe the prediction error of concentration combination from a certain mixture, which is calculated in our case as: $RMSE(C,\ \hat{C}) = \sqrt{\frac{1}{2} * [(C_{\mathrm{IPA}} - \hat{C}_{\mathrm{IPA}})^2 + (C_{\mathrm{Eth}} - \hat{C}_{\mathrm{Eth}})^2]}$, where C_{IPA} and C_{Eth} denote the predicted component concentration of IPA and ethanol, while $\hat{C}_{\mathrm{IPA}}$ and $\hat{C}_{\mathrm{Eth}}$ are the corresponding true component concentrations, respectively. Figure 5d(iv) illustrates the RSME of the predicted concentration combinations of the test dataset ranging from 2.7 to 9.1 ppm, of which 60% are smaller than 5 ppm, and 40% are within 5–10 ppm. The precise prediction of mixture concentrations with low error values is based on the accurate spectrum decomposition achieved by the trained MLP regressor. We need to clarify here that the labels used are a series of 50-dimensional vectors (spectrum values of 25 wavelength points for IPA and corresponding values for ethanol at the same 25 wavelength points). This means that the spectra of acetone are also completely unknown to the MLP model. In practical applications, the situations are more complex and the gas to be detected may contain unknown components. The measured MIR spectra will be affected, as they represent the spectra of a mixture of the target gas and the unknown components. However, the intrinsic molecular fingerprints of the target gas remain unchanged, which arise from the vibrations of molecules. Therefore, the spectra of the target gas can be recovered using the same training process as we demonstrated here. We can collect the pure-form spectra of the target gas using our devices in the experiment room and then perform the standard training process. After that, our devices can be used in practical cases to recover the spectra of the gas to be detected and predict the concentrations with high accuracy, even if the target gas contains unknown components. The performance comparison of our AI-enhanced "photonic nose" with recent "electronic nose" and photonic VOC sensors is listed in Note S15 (Supporting Information). In real-world environments, gas mixtures may contain various gases, introducing multiple interferences. However, there are always dominant gases, with many others being minor components. Therefore, we only need to collect the spectra of the pure-form dominant gases. By using these spectral data as target outputs during the training process, we can achieve spectrum decomposition of mixture spectra and predict the concentration of dominant gases in practical applications, even under interference from minor gases.

2.6. Monitoring of Wine Fermentation Process Using Proposed "Photonic Nose"

In wine production, a critical stage involves fermenting the grapes to convert the sugars into ethanol in an oxygen-free and clean environment, which is essential to maintaining high quality and delicious results. In the field of smart agriculture, it is imperative to achieve fast, environmentally friendly, and noninvasive fermentation monitoring. **Figure 6**a,b demonstrates the flow chart of our fermentation monitoring. The photographs of fermentation solutions at different fermentation times are illustrated in Figure S14 (Supporting Information). Pure nitrogen served as a buffered gas, flowing into the fermentation solution to generate vapor, which was then directed through the outlet into the gas cell housing our MCMRPN platform. Through spectral analysis of the collected data, valuable insights into the fermentation process and its quality can be gleaned. Figure 6c,d demonstrates the calibrated absorbance spectrum of fermentation solution and ethanol solution, respectively (see calibration details in Figure S14, Supporting Information). The ethanol solution ranging from 1% to 6% is in the unit of vol%. The absorbance peaks of fermentation products are observed and gradually increase as the fermentation time increases. Furthermore, the spectra of the fermentation solution are similar to the ones of the ethanol solution, which confirms that the main product of our fermentation is ethanol. Figure 6e plots the peak values at 9.49 µm extracted from Figure 6c,d, respectively. Peak values of the fermentation solution increase in the early stage (Day 1 and Day 2) and then toward stability, which means that fermentation proceeds vigorously at first and then gradually slows to a standstill. Highly toxic byproducts methanol may be produced in practice due to the pollution of unclean raw materials or other bacteria. Many unscrupulous merchants increase the content of alcohol by adding methanol that far exceeds safe standards because methanol is much cheaper than ethanol. Therefore, it is needed to detect the methanol during the fermentation process and wine products to avoid safety issues. We measured the spectra of the vapor of fermentation solution, the mixtures of fermentation solution and methanol, as well as the mixtures of fermentation solution and ethanol (Figure S10,

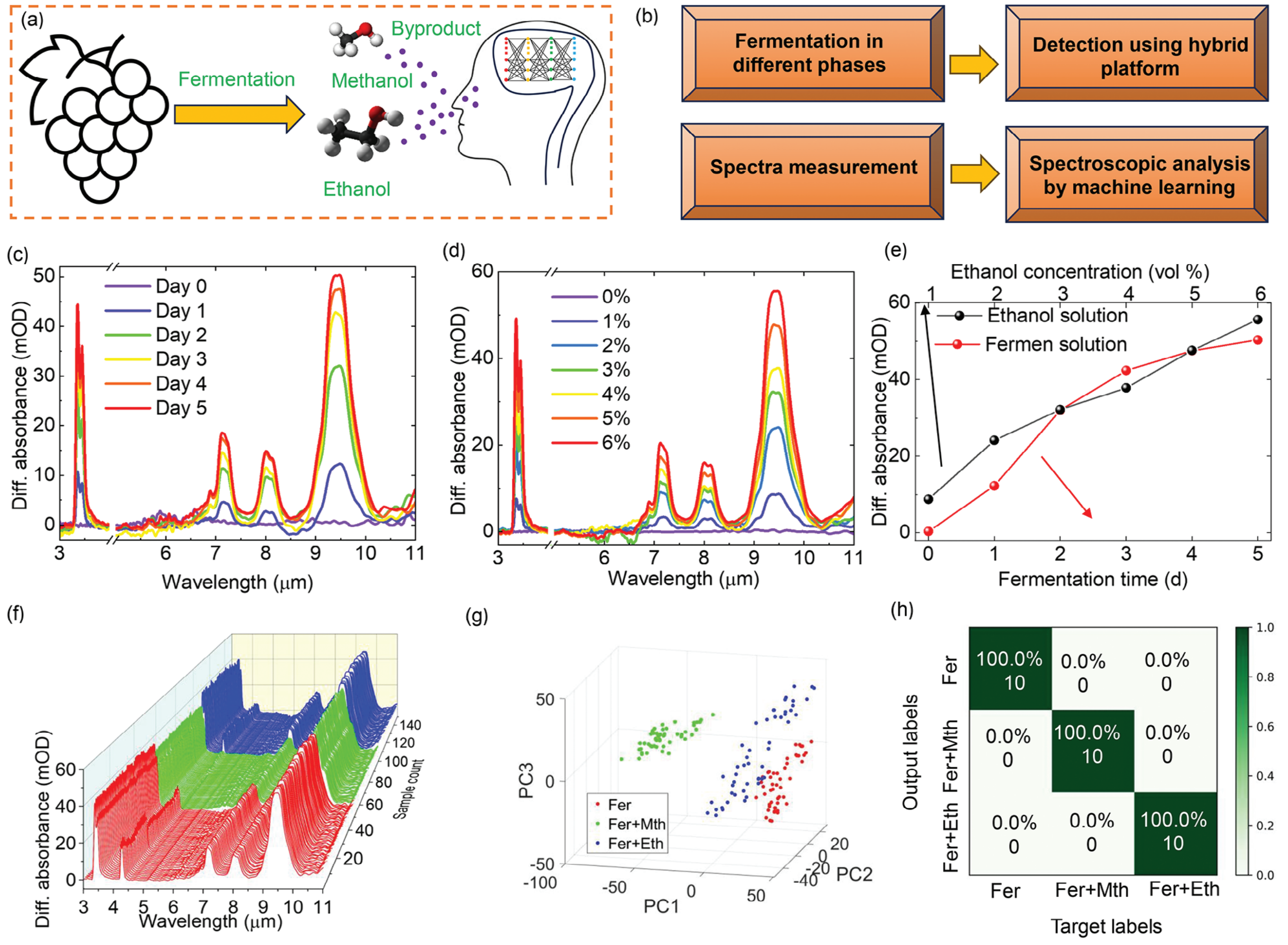

Figure 6. Monitoring of wine fermentation process using proposed "photonic nose". a) Schematic diagram of working mechanism of fermentation monitoring. b) Workflow of fermentation monitoring. c) Measured absorbance spectra (after calibration) of the vapor of the fermentation solution. d) Measured absorbance spectra of the vapor of ethanol solution with varying volume ratios. e) The extracted peak values at 9.49 μm of the spectra in (c, d), respectively. f) Measured spectra of vapor of fermentation solution, the mixture of fermentation solution and methanol solution, and the mixture of fermentation solution and ethanol solution. g, h) the 3D plots of PCA of spectra data of (f), and the respective testing accuracy using spectrum data in (f) with CNN.

Supporting Information). The three solutions were prepared to have a similar alcohol concentration. Figure 6f demonstrates the 50 × 3 spectra of three solutions (each solution was measured 50 times to obtain a sufficient training data set). A PCA model was applied to differentiate these spectra. The results of PCA are plotted in Figure 6g. Three groups of respective three solutions are well distinguished. Furthermore, a high accuracy of 100% is achieved in classifying the spectra in Figure 6f by applying a CNN model (Figure 6h).

3. Conclusion

In conclusion, we propose an AI-enhanced "photonic nose" for high-accuracy classification and low-deviation component concentration prediction for trace VOC gas mixtures (IPA, ethanol, and acetone and their combinations). An MCMRPN platform is designed to cover molecular fingerprints in the MIR range and spin-coated with a layer of MOF as the gas enrichment layer. The gas sensing performance of our MCMRPN platform is demonstrated with three widely used VOC molecules and low LoDs down to single-digit ppm are achieved (IPA: 1.99 ppm, ethanol: 3.43 ppm, acetone: 9.82 ppm). Based on these low LoD results, we explore molecular identification for trace VOC gas mixtures with the assistance of deep machine learning. A high classification accuracy of 100% is achieved with a CNN model for 125-class (5 × 5 × 5) mixtures with varying mixing ratios of IPA (5 concentrations ranging from 0 to 130 ppm), ethanol (5 concentrations ranging from 0 to 130 ppm), and acetone (5 concentrations ranging from 0 to 201 ppm). An alternative MLP regression model is employed to perform the spectrum decomposition. By training on the spectral information of only 80% of the concentration combinations, we successfully decompose the spectra from the remaining 20% unknown mixing combinations into spectra of pure forms of components. Based on the MLP-decomposed spectra, a linear regression model is utilized for concentration prediction of selected components of interest (IPA and ethanol).

Low deviation prediction results within 10 ppm RMSE range are achieved for IPA and ethanol both in the range of 0–130 ppm under interference from 50 ppm acetone. Additionally, molecular fingerprints of VOCs are dense in the range of 7–10 µm. For our MCMRPN, the resonant wavelength at 7.8 µm wavelength under horizontal polarization complements the gap between two resonant wavelengths at 6.0 and 8.9 µm under vertical polarization. Our MCMRPN platform holds the potential to extract the Supporting Information by simply altering the incident polarization to 0° for machine learning (Figure S11, Supporting Information). Our work paves the way for next-generation intelligent "photonic nose" in a wide range of applications including environmental monitoring and smart farming applications.

4. Experimental Section

Fabrication: The CaF_2 chip underwent an initial rinsing with acetone and an IPA solution, employing sonication for 1 min. Subsequently, it was subjected to oxygen plasma treatment to ensure the uniform formation of PMMA. The photoresist, 495K PMMA A4, was then spin-coated at 4000 rpm for 1 min. To prevent charge accumulation, an additional layer of E-spacer laser was spin-coated on top of the PMMA. The metal nanoantenna was patterned using E-beam lithography (EBL, Jeol). This was followed by development in MIBK:IPA (1:3) for 30 s and rinsing in IPA for an additional 30 s. After the EBL pattern was established, a deposition of 5-nm Ti and 80-nm Au was carried out using an E-Beam Evaporator (AJA), followed by a standard lift-off process. In terms of the MOF (ZIF-67) modification, it began with the preparation of MOF (purchase from ACS Material LLC) solutions in methanol. Then, it was sonicated for 10 min at 50% energy in an ultrasonic cleaner to obtain fine crystals. Then, the MOFs were spin-coated onto the device surface to complete the preparation of the MOF-hybrid platform.

Simulation: The numerical simulations in this work were carried out using the finite-difference time-domain (FDTD) method (Lumerical Inc.). The far-filed transmission spectrum and near-filed distributions were extracted by using two frequency-domain fields and power monitors. A plane wave with normal incidence served as the light source, with polarization set at either 0° or 90°. The refractive index of CaF_2 was established at 1.38. Periodic boundary conditions were implemented in the x and y directions, while a perfectly matched layer (PML) boundary condition was applied in the z direction.

TCMT Modeling: The temporal coupled-mode theory (TCMT) is used to model the resonance of the CMRPN and the coupling between the middle nanorod and the double-u nanoantenna under vertical excitation. The fitting is done by a MATLAB code.

FTIR Measurement: The spectral response was assessed using a Fourier-transform infrared (FTIR) microscope (Agilent Cary 660) equipped with an FTIR spectrometer (Agilent Cary 620) and a liquid-nitrogen-cooled mercury cadmium telluride detector. The measurement area was defined as 200×200 µm^2, with each measurement employing 30 scans.

Gas Sensing: In the gas sensing measurements, nitrogen (N_2) was chosen as the buffer gas and divided into two streams. One stream comprised pure N_2, while the other was directed into a pure VOC solution (IPA, ethanol, or acetone) to generate a VOC-N_2 mixture. Both the VOC gas and N_2 entered the mixing chamber through the air inlet, swiftly blending uniformly thanks to a fan in the mixing chamber, and ultimately exited through the air outlet. The concentration of VOC gas in the dilution was precisely and dynamically controlled by adjusting the mass flow controllers (MFC) in both streams, a calibration achieved using commercial sensors designed for VOCs. The uniformly mixed VOC-N_2 gas mixture then flowed into the gas cell where the chip was positioned. This gas cell featured upper and lower CaF_2 IR transparent windows. The differential absorbance spectra of VOCs were computed as $-\log_{10}(T/T_0)$, where T and T_0 represented the measured VOC spectrum and measured reference spectrum using pure N_2, respectively.

Deep Learning Methods: CNN models are applied for the classification of gas mixtures, employing a categorical cross-entropy function as the loss function and utilizing adaptive moment estimation (Adam) as the optimizer. PCA is employed for classifying gas mixtures of several classes. Spectrum decomposition of a mixture is accomplished using the MLP regressor, and the prediction of component concentrations is executed through linear regressor models. All machine learning models were implemented in Python 3.11 with PyTorch.

Fermentation Monitoring: Fresh grapes were first washed clean and then placed into a glass container. Subsequently, the grapes are submerged in water, with dry household yeast powder added to simulate industrial production conditions. Pure nitrogen serves as a buffered gas, flowing into the fermentation solution to generate vapor, which is then directed through the outlet into the gas cell housing the MCMRPN platform. Through spectral analysis of the collected data, valuable insights into the fermentation process and its quality can be gleaned.

Supporting Information

Supporting Information is available from the Wiley Online Library or from the author.

Acknowledgements

J.X. and Z.R. contributed equally to this work. This work was supported by the Ministry of Education (MOE) Singapore Tier 2 project (MOE-T2EP50220-0014), the Advanced Research and Technology Innovation Centre (A-0005947 20-00) at NUS, Singapore, Agency for Science, Technology and Research (A*STAR, A18A4b0055), and Reimagine Research Scheme (RRSC, A-0009454-01-00).

Conflict of Interest

The authors declare no conflict of interest.

Data Availability Statement

The data that support the findings of this study are available from the corresponding author upon reasonable request.

Keywords

artificial intelligence, gas sensors, metamaterials, mid-infrared spectroscopy, volatile-organic-compound mixture analysis

Received: June 13, 2024
Revised: July 30, 2024

---

[1] R. Vishinkin, H. Haick, *Small* **2015**, *11*, 6142.
[2] J. Zhu, Z. Ren, C. Lee, *ACS Nano* **2021**, *15*, 894.
[3] Z. Du, S. Zhang, J. Li, N. Gao, K. Tong, *Appl. Sci.* **2019**, *9*, 338.
[4] A. Kansal, *J. Hazard Mater.* **2009**, *166*, 17.
[5] Y. Huang, T. Zhang, G.-X. Wang, Y.-X. Xing, S.-L. He, *Appl. Phys. Lett.* **2023**, *122*, 111105.
[6] D. Li, B. Zhu, K. Pang, Q. Zhang, M. Qu, W. Liu, Y. Fu, J. Xie, *ACS Sens.* **2022**, *7*, 1555.
[7] W. Y. Chen, X. Jiang, S.-N. Lai, D. Peroulis, L. Stanciu, *Nat. Commun.* **2020**, *11*, 1302.

[8] Y. K. Jo, S.-Y. Jeong, Y. K. Moon, Y.-M. Jo, J.-W. Yoon, J.-H. Lee, *Nat. Commun.* **2021**, *12*, 4955.

[9] R. A. Potyrailo, S. Go, D. Sexton, X. Li, N. Alkadi, A. Kolmakov, B. Amm, R. St-Pierre, B. Scherer, M. Nayeri, *Nat. Electronics* **2020**, *3*, 280.

[10] D. Sim, Z. Kuang, G. Sant'Anna, R. M. Krabacher, M. C. Brothers, J. L. Chávez, J. A. Martin, A. E. Islam, B. Maruyama, R. R. Naik, *Adv. Mater. Interfaces* **2023**, *10*, 2201707.

[11] H. Ji, W. Qin, Z. Yuan, F. Meng, *Sens. Actuators, B* **2021**, *348*, 130698.

[12] F. Meng, X. Shi, Z. Yuan, H. Ji, W. Qin, Y. Shen, C. Xing, *Sens. Actuators, B* **2022**, *350*, 130867.

[13] H. Ji, C. Mi, Z. Yuan, Y. Liu, H. Zhu, F. Meng, *IEEE Trans. Ind. Electron.* **2022**, *70*, 6395.

[14] G. S. Kulkarni, K. Reddy, Z. Zhong, X. Fan, *Nat. Commun.* **2014**, *5*, 4376.

[15] G. Antonacci, J. Goyvaerts, H. Zhao, B. Baumgartner, B. Lendl, R. Baets, *APL Photonics* **2020**, *5*, 081301.

[16] G. Niu, Y. Zhuang, Y. Hu, Z. Liu, B. Wu, F. Wang, *Surf. Interfaces* **2024**, *44*, 103761.

[17] D. Li, H. Zhou, Z. Chen, Z. Ren, C. Xu, X. He, T. Liu, X. Chen, H. Huang, C. Lee, X. Mu, *Adv. Mater.* **2023**, *35*, 2301787.

[18] A. John-Herpin, A. Tittl, L. Kuhner, F. Richter, S. H. Huang, G. Shvets, S. H. Oh, H. Altug, *Adv. Mater.* **2022**, *35*, 2110163.

[19] H. Zhou, D. Li, Z. Ren, X. Mu, C. Lee, *InfoMat* **2022**, *4*, e12349.

[20] A. L. Andreas Tittl, M. Liu, F. Yesilkoy, D.-Y. Choi, D. N. Neshev, Y. S. Kivshar, H. Altug, *Science* **2018**, *360*, 1105.

[21] N. Liu, M. L. Tang, M. Hentschel, H. Giessen, A. P. Alivisatos, *Nat. Mater.* **2011**, *10*, 631.

[22] R. Adato, S. Aksu, H. Altug, *Mater. Today* **2015**, *18*, 436.

[23] X. Tan, H. Zhang, J. Li, H. Wan, Q. Guo, H. Zhu, H. Liu, F. Yi, *Nat. Commun.* **2020**, *11*, 5245.

[24] F. Schuknecht, K. Kołątaj, M. Steinberger, T. Liedl, T. Lohmueller, *Nat. Commun.* **2023**, *14*, 7192.

[25] R. Wilcken, J. Nishida, J. F. Triana, A. John-Herpin, H. Altug, S. Sharma, F. Herrera, M. B. Raschke, *Proc. Natl. Acad. Sci. USA* **2023**, *120*, 2220852120.

[26] D. Lu, G. Zhu, X. Li, J. Xiong, D. Wang, Y. Shi, T. Pan, B. Li, L. P. Lee, H. Xin, *Nat. Photonics* **2023**, *17*, 904.

[27] D. Rodrigo, A. Tittl, N. Ait-Bouziad, A. John-Herpin, O. Limaj, C. Kelly, D. Yoo, N. J. Wittenberg, S. H. Oh, H. A. Lashuel, H. Altug, *Nat. Commun.* **2018**, *9*, 2160.

[28] H. Zhou, X. Hui, D. Li, D. Hu, X. Chen, X. He, L. Gao, H. Huang, C. Lee, X. Mu, *Adv. Sci.* **2020**, *7*, 2001173.

[29] Z. Ren, Z. Zhang, J. Wei, B. Dong, C. Lee, *Nat. Commun.* **2022**, *13*, 3859.

[30] Z. Ren, Z. Dang, C. Lee, 2020 IEEE 33rd International Conference on Micro Electro Mechanical Systems (MEMS), Vancouver, BC, Canada, *2020*, pp. 725-728.

[31] H. Zhou, Z. Ren, D. Li, C. Xu, X. Mu, C. Lee, *Nat. Commun.* **2023**, *14*, 7316.

[32] H. Zhou, D. Li, Z. Ren, C. Xu, L.-F. Wang, C. Lee, *Sci. Adv.* **2024**, *10*, eado3179.

[33] C. Xu, Z. Ren, H. Zhou, J. Zhou, D. Li, C. Lee, *Adv. Funct. Mater.* **2023**, *34*, 2314482.

[34] S. Rosas, K. A. Schoeller, E. Chang, H. Mei, M. A. Kats, K. W. Eliceiri, X. Zhao, F. Yesilkoy, *Adv. Mater.* **2023**, *35*, 2301208.

[35] F. Neubrech, A. Pucci, T. W. Cornelius, S. Karim, A. García-Etxarri, J. Aizpurua, *Phys. Rev. Lett.* **2008**, *101*, 157403.

[36] D. Yoo, F. de León-Pérez, M. Pelton, I.-H. Lee, D. A. Mohr, M. B. Raschke, J. D. Caldwell, L. Martín-Moreno, S.-H. Oh, *Nat. Photonics* **2021**, *15*, 125.

[37] D. Yoo, D. A. Mohr, F. Vidal-Codina, A. John-Herpin, M. Jo, S. Kim, J. Matson, J. D. Caldwell, H. Jeon, N.-C. Nguyen, *Nano Lett.* **2018**, *18*, 1930.

[38] L. Zhu, D. Shen, K. H. Luo, *J. Hazard. Mater.* **2020**, *389*, 122102.

[39] Y. Hua, Y. Ahmadi, K. H. Kim, *Environ. Pollut.* **2022**, *311*, 119931.

[40] L. Hu, W. Cheng, W. Zhang, F. Wu, S. Peng, J. Li, *J. Porous Mater.* **2017**, *24*, 541.

[41] Z. Guo, J. Huang, Z. Xue, X. Wang, *Chem. Eng. J.* **2016**, *306*, 99.

[42] S.-C. Hsu, C. Lu, *J. Air Waste Manag. Assoc.* **2009**, *59*, 990.

[43] Z. Zhai, Y. Sun, X. Hao, C. Li, *Appl. Surf. Sci.* **2023**, *621*, 156833.

[44] S. Kutluay, F. Temel, *Colloids Surf., A* **2021**, *609*, 125848.

[45] D. Fu, J. Chung, Q. Liu, R. Raziq, J. S. Kee, M. K. Park, S. Valiyaveettil, P. Lee, *Sens. Actuators, B* **2018**, *257*, 136.

[46] T. Zhou, Y. Sang, Y. Sun, C. Wu, X. Wang, X. Tang, T. Zhang, H. Wang, C. Xie, D. Zeng, *Langmuir* **2019**, *35*, 3248.

[47] H. Zhou, Z. Ren, C. Xu, L. Xu, C. Lee, *Nano-Micro Lett.* **2022**, *14*, 207.

[48] F. Mumtaz, B. Zhang, N. Subramaniyam, M. Roman, P. Holtmann, A. P. Hungund, R. O'Malley, T. M. Spudich, M. Davis, R. E. Gerald Ii, J. Huang, *ACS Appl. Mater. Interfaces* **2024**, *16*, 13071.

[49] A. John-Herpin, D. Kavungal, L. von Mucke, H. Altug, *Adv. Mater.* **2021**, *33*, 2006054.

[50] A. Tittl, A. John-Herpin, A. Leitis, E. R. Arvelo, H. Altug, *Angew. Chem., Int. Ed. Eng.* **2019**, *58*, 14810.

[51] Z. Zhang, X. Liu, H. Zhou, S. Xu, C. Lee, *Small Struct.* **2023**, *5*, 2300325.

[52] L. Kuhner, R. Semenyshyn, M. Hentschel, F. Neubrech, C. Tarin, H. Giessen, *ACS Sens.* **2019**, *4*, 1973.

[53] Y. Zhuang, D. Yin, L. Wu, G. Niu, F. Wang, *APL Mach. Learn.* **2024**, *2*, 016104.

[54] D. Li, W. Liu, B. Zhu, M. Qu, Q. Zhang, Y. Fu, J. Xie, *ACS Sens.* **2022**, *7*, 2767.

[55] D. Li, Z. Xie, M. Qu, Q. Zhang, Y. Fu, J. Xie, *ACS Appl. Mater. Interfaces* **2021**, *13*, 47043.

[56] J. Zhou, Z. Zhang, B. Dong, Z. Ren, W. Liu, C. Lee, *ACS Nano* **2023**, *17*, 711.

[57] G. A. R. Sampedro, S. M. Rachmawati, D.-S. Kim, J.-M. Lee, *Sensors* **2022**, *22*, 9446.

[58] J. Zhu, S. Ji, Z. Ren, W. Wu, Z. Zhang, Z. Ni, L. Liu, Z. Zhang, A. Song, C. Lee, *Nat. Commun.* **2023**, *14*, 2524.

[59] Y. X. Leong, Y. H. Lee, C. S. L. Koh, G. C. Phan-Quang, X. Han, I. Y. Phang, X. Y. Ling, *Nano Lett.* **2021**, *21*, 2642.

[60] X. Liu, Z. Zhang, J. Zhou, W. Liu, G. Zhou, C. Lee, *Small* **2024**, 2400035.

[61] Y. Zhuang, X. Liu, X. Wang, G. Niu, R. Cheng, F. Wang, *IEEE Sens. Lett.* **2023**, *7*, 1.

[62] D. Li, G. Liu, Q. Zhang, M. Qu, Y. Q. Fu, Q. Liu, J. Xie, *Sens. Actuators, B* **2021**, *331*, 129414.

[63] P. Qin, B. A. Day, S. Okur, C. Li, A. Chandresh, C. E. Wilmer, L. Heinke, *ACS Sens.* **2022**, *7*, 1666.

[64] I. Cho, K. Lee, Y. C. Sim, J. S. Jeong, M. Cho, H. Jung, M. Kang, Y. H. Cho, S. C. Ha, K. J. Yoon, I. Park, *Light: Sci. Appl.* **2023**, *12*, 95.

[65] M. Chen, M. Zhang, Z. Yang, C. Zhou, D. Cui, H. Haick, N. Tang, *Adv. Funct. Mater.* **2024**, *34*, 2309732.